Attractions between Hard Colloidal Spheres in Semiflexible Polymer Solutions

Ritu Verma, J. C. Crocker, T. C. Lubensky, and A. G. Yodh*

Department of Physics and Astronomy, University of Pennsylvania, 209 S. 33rd Street, Philadelphia, Pennsylvania 19104-6396

Received March 10, 1999; Revised Manuscript Received October 15, 1999

ABSTRACT: We explore the depletion attractions that arise between hard colloidal spheres immersed in a nonadsorbing polymer solution of DNA. We spatially confine two 1.25 μm silica spheres in a scanning optical tweezer and quantitatively examine their interaction potential in double-stranded DNA solutions of different concentrations. The potentials obtained display variations in depth and range that are consistent with scaling behavior expected for semiflexible polymers near the θ-point. In particular, we clearly observe the crossover from a dilute solution of Gaussian coils to the weakly fluctuating semidilute regime dominated by two-point collisions (Schaefer, D. W.; Joanny, J. F.; Pincus, P. *Macromolecules* **1980**, *13*, 1280−1289). We also quantitatively test the Asakura−Oosawa model for these systems and show that it may be used in both the semidilute as well as the dilute regime. At fixed DNA concentration, we find that the range and depth of the interparticle potentials do not change significantly for ionic concentrations between 1 and 50 mM.

I. Introduction

Colloid−polymer mixtures form the basic ingredients of a wide variety of systems ranging from frozen desserts and motors oils to living cells. The structural and dynamical properties of these complex fluids ultimately depend on the microscopic interactions between suspension constituents and are of fundamental interest.[1] In this contribution we explore the forces between nearly hard-sphere silica particles in a model colloid−polymer mixture. The polymer we employ in our experiments is bacteriophage lambda DNA (λ-DNA), a monodisperse, nonadsorbing, semiflexible polymer with a persistence length of ≈50 nm and a contour length of 16.5 μm. The model system makes possible detailed microscopic observations of polymer-induced colloidal interactions in a regime where particle and polymer effective sizes are similar. It also enables us to probe the bulk behavior of semiflexible polymers as a function of concentration.[2]

What are the forces between hard spheres in a nonadsorbing polymer solution? Theoretical progress on this problem began in the late 1950s with the depletion model of Asakura and Oosawa (AO)[3,4] for a dilute gas of small polymer coils treated as hard spheres mixed with relatively large colloidal particles. The AO model predicts a polymer-mediated attractive interaction between spheres. In semidilute solutions, where the polymer correlation length is much smaller than the particle diameter, an attraction between particles is predicted based on mean-field and scaling theory.[5] Calculations that treat polymer configurations and polymer−polymer interactions more realistically than the AO model have been published.[6−9] Computer simulations[10,11] and integral methods[12,13] have also been employed to understand these interactions. With the exception of refs 5, 8, and 14, most theoretical work on colloid−polymer systems has been restricted to regimes in which the polymer solution is dilute.

Experimental investigations of these interactions have been indirect or limited in scope. Studies of the phase behavior of colloid−polymer mixtures[15] are examples of experiments that provide indirect evidence of these forces. Direct measurements using radiation pressure forces[16] and the surface force apparatus (in living polymers)[17] have determined the magnitudes of these forces in specific geometries. Measurements using total internal reflection microscopy[18] and atomic force microscopy[19] have revealed the potential between particles and walls in dilute systems, and neutron-scattering experiments[20] have indirectly inferred the nature of these interactions from changes in differential scattering cross sections. A nontraditional approach[21] using lipid bilayer membranes has also been used to probe the range of the depletion effect. The measurements we present are the first to probe the functional form of the polymer depletion interaction affecting two particles in suspension over a broad range of polymer concentrations from dilute to semidilute. Our work focuses on semiflexible polymers, which might be expected to differ from flexible polymers, and a complete understanding of the data will ultimately require a theory of colloid−polymer mixtures in the intermediate size range where the polymer correlation length and particle diameter are comparable.

We introduce a novel optical technique that allows us to trap two particles in a line-scanned optical tweezer and to directly visualize the relative motions of these two particles. From these observations and the probability distributions derived thereof, we deduce a functional form for the particle interaction potential, which can then be used to quantitatively test different models. We have investigated the range and the depth of the interaction potential between the spheres as the background polymer concentration and background salt concentration are varied. We explore both dilute and semidilute polymer solutions. By quantitatively following the trends in our data, we are able to measure the properties of λ-DNA in dilute and crowded environments. Theoretical studies[22,23] have highlighted the existence of new phases as the stiffness parameter of the polymer is increased. We find clear evidence for the existence of one such phase, the weakly fluctuating semidilute phase, that has not been cleanly observed

10.1021/ma990362v CCC: $19.00
Published on Web 12/17/1999

before. These results clearly demonstrate the capability of this new technique to probe polymer properties in the submicrometer range.

The purpose of this paper is to present a coherent and more complete picture of work that has been described briefly in a short publication.[2] The paper is organized as follows. In section II we review the key theoretical features of semiflexible polymers that are required to understand the implications of our potential measurements for polymer phase behavior, and we review the AO and mean-field theories for the forces that arise between particles in polymer solutions. In the latter case we explicitly connect the mean-field results to the conventional AO model. In section III we review experimental details. The discussion of the data analysis is much more complete than that done earlier, and some examples of unprocessed potentials are given. In section IV we describe and discuss the full set of results we have obtained. In addition to presenting the potential and scaling data provided in the earlier report,[2] we describe measurements of the potential as a function of background salt concentration and as a function of particle size. We also show explicitly where the parameters of our experimental systems lie in the context of the phases of the semiflexible polymer. A brief conclusion is presented in section V.

II. Theory

A. Phases and Structure of Polymer Solutions. Ideal flexible polymers can be modeled as a sequence of N freely joined spherical beads of diameter d.[23,24] In a θ-solvent where interactions between beads vanish, a flexible polymer is an ideal Gaussian chain with a radius of gyration R that scales as $N^{1/2}d$. The freely joined bead model is a convenient theoretical idealization. Any real polymer is, however, composed of a series of monomer units connected by links whose directions are correlated out to some persistence length l_p. If each monomer unit has width d and length b, then a given polymer has a contour length $L = N_m b$, where N_m is the number of monomer units. In the idealized freely joined bead model, $d = b$, $N = N_m$, and $L = Nd$. In general, however, the polymer width d equals neither the monomer length b nor the persistence length l_p, and one can choose to describe a polymer in terms of its monomer number N_m, in terms of its bead number $N = L/d$, or by $N_{eff} = L/2l_p$, the number of Kuhn lengths $l = 2l_p$ it contains. Polymer flexibility is characterized by a rigidity parameter $p = l/d$. In flexible polymers $p = 1$, and in semiflexible polymers $p > 1$. Since the direction of each Kuhn segment is independent of that of its neighbors, the square of the radius of gyration of a semiflexible polymer in a θ-solvent is given by $R_\theta^2 = N_{eff} l^2 = Ll = pNd^2 = N_m bl$. Thus, for a given N and d, the radius of gyration of a semiflexible polymer is $\sqrt{p}$ times as large as that of a flexible polymer with $p = 1$.

In dilute polymer solutions at temperatures T near the θ-temperature, the polymer osmotic pressure can be expanded in a virial series in the bead concentration $c = Nn_p$ where n_p is the polymer coil concentration

$$\frac{\Pi}{k_B T} = \frac{c}{N} + B_c c^2 + 2C_c c^3 \quad (1)$$

$$= n_p + BN_{eff}^2 n_p^2 + 2CN_{eff}^3 n_p^3 \quad (2)$$

where $B_c \sim d^3\tau$, with $\tau = (T - \theta)/\theta$, is the second virial coefficient and $C_c \sim d^6$ is the third virial coefficient. The above equation is obtained from eq 1 by setting $N_{eff} = N/p$ and $c = n_p N$ to yield $B = p^2 B_c \sim l^2 d\tau \sim p^{-1} l^3 \tau$ and $C = p^3 C_c \sim l^3 d^3$.

As τ increases, collisions between monomers within a polymer become important, even in the dilute limit, and polymers undergo self-avoiding rather then Gaussian walks. A dimensionless measure of the strength of self-avoidance is provided by the number of contacts between monomers in a Gaussian chain, $z = 2(3/2\pi)^{3/2} N^{1/2} B_c / p^{3/2} d^3 \sim B_c N^2 / R^3$. If $z > 1$, self-avoidance is important, the polymer swells, and in the dilute limit $R \sim p^{1/5} \tau^{1/5} N^{3/5} d$; if $z < 1$, self-avoidance is unimportant, and the polymer is effectively Gaussian with $R = \alpha(Ll)^{1/2}$, where $\alpha^2 \approx 1 + 4z/3$.[23] Note that z, through its dependence on R, depends on the rigidity parameter p. For a fixed N, z decreases with increasing p.

We will try to understand our data in the context of a phase diagram[22,23] in the $cd^3 - \tau$ plane for semiflexible polymers with $p > 1$. To this end, we begin with eq 1, which provides a correct description of the osmotic pressure for *both* flexible and semiflexible polymers at small values of z. From it, we can identify three distinct regions of the phase diagram (Figure 1a) defined by which of the three terms in the power series in c dominates. In region I, the linear term dominates, and the osmotic pressure is $\Pi_I \sim c/N$. In region V, the cubic term dominates, and $\Pi \sim C_c c^3$. The boundary between regions I and V occurs at $cd^3 \sim N^{-1/2}$ where $\Pi_I = \Pi_V$. In region VI, the quadratic term dominates and $\Pi_{VI} \sim d^3 \tau c^2$. The I−VI boundary occurs at $cd^3 \sim \tau^{-1} N^{-1}$, and the VI−VII boundary occurs at $cd^3 \sim \tau$. The three boundaries meet at the point $P_1 \equiv (c_1 d^3, \tau_1) = (N^{-1/2}, N^{-1/2})$.

As concentration increases, chains begin to overlap above a concentration $c^* \sim N/R^3$. For $c > c^*$ but $cd^3 \ll 1$, the system is semidilute. When $z < 1$ and Gaussian statistics apply, $c^* d^3 \sim N^{-1/2} p^{-3/2}$. Thus, the line $cd^3 = N^{-1/2} p^{-3/2} \leq N^{-1/2}$ separates dilute from semidilute solutions and divides region I into two regions I and VII. Region I, the dilute Gaussian region, is limited to $c < c^*$. Region VII lies between region I and regions V and VI and has an osmotic pressure, $\Pi \sim c/N$, equal to that of a dilute solution even though there is chain overlap. Polymers in region I and VII behave like noninteracting Gaussian coils with radii of gyration $R_I \sim p^{1/2} N^{1/2} d$. Note that as $p \to 1$ region VII vanishes. Both regions V and VI are in the semidilute regime in which particle interactions can be treated perturbatively. They are characterized by a correlation length ξ representing the mean distance between enlargement lengths. In region V, $\xi_V \sim d(cd^3)^{-1}$, and in region VI, $\xi_{VI} = l_p (6BN_{eff} n_p)^{-1/2} \sim (cd^3)^{-1/2} \tau^{-1/2} p^{1/2} d$. (The usual expression for ξ in region VI is $\xi = a(24B_c c)^{1/2}$, where $a = bl^{1/2}$. By using the fact that $a^2 = l^2/p$, we regain the equation in the text.)

The phase diagram, (Figure 1a), based on eq 1 is only valid for $z < 1$ or for $\tau < p^{3/2} N^{-1/2}$. At larger τ, self-avoidance becomes important, and the osmotic pressure and characteristic lengths become scaling functions of c/c^* at least for c/c^* not too large, where $c^* d^3 \sim p^{-3/5} \tau^{-3/5} N^{-4/5}$ is the semidilute crossover concentration appropriate to swollen polymers. The osmotic pressure satisfies a scaling form $\Pi/k_B T = (c/N) f(c/c^*)$. We can now identify two new regions of the phase diagram (Figure 1b): the swollen dilute region II and the fluctuating semidilute region IV. The boundary

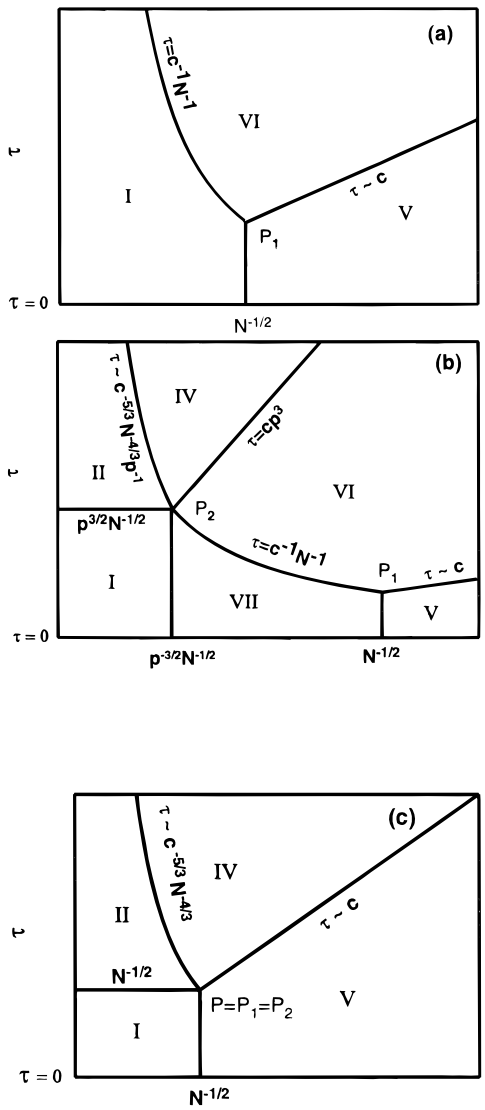

Figure 1. (a) Polymer phase diagram near the θ-point where self-avoidance is unimportant. This diagram follows from eq 1 valid for both flexible and semiflexible polymers. It shows the Gaussian dilute phase I and the weakly fluctuating semidilute phases V and VI dominated, respectively, by three-point and two-point collisions. (b) Full phase diagram for semiflexible polymers. This diagram is obtained from that of (a) by superposing phases resulting from self-avoidance interactions and semidilute overlap. The new phases are the non-Gaussian dilute phase II, the strongly fluctuating semidilute phase IV, and the Gaussian semidilute phase VII. (c) Phase diagram for flexible polymers. The points of the semiflexible phase diagram $P_1 = (c_1d^3, \tau_1) = (N^{-1/2}, N^{-1/2})$ where phases V, VI, and VII meet and $P_2 = (p^{-3/2}N^{-1/2}, p^{3/2}N^{-1/2})$ where phases I, II, and IV meet merge to eliminate phase VI and VII from the flexible-polymer phase diagram.

between region I and region II is defined by $z \sim 1$ or $\tau \sim p^{3/2}N^{-1/2}$ and that between II and IV by $c \sim c^*$ or $\tau \sim p^{1/3}(cd^3)^{-5/3}N^{-4/3}$. Since the curve $c = c^*$ (τ) must be continuous, the I−II, II−IV, and I−VII boundaries must meet at the point $P_2 = (c_2d^3, \tau_2) = (p^{-3/2}N^{-1/2}, p^{3/2}N^{-1/2})$. The VII−VI boundary also terminates at P_2. In the dilute region II, $R_{II} \sim dp^{1/5}\tau^{1/5}N^{3/5}$ and $\Pi_{II}/k_BT \sim (c/N) + AR_{II}^3(c/N)^2$, where A is a constant. In the semidilute region IV, $\Pi_{IV} \sim c(cd^3)^{5/4}\tau^{3/4}p^{3/4} \sim c^{9/4}$, and the correlation length is $\xi_{IV} \sim d(cd^3)^{-3/4}\tau^{-1/4}p^{-1/4}$. The transition from the strongly fluctuating semidilute region IV to the weakly fluctuating semidilute region VI occurs when their osmotic pressures become equal, i.e., when $p^{3/4}c^{9/4}\tau^{3/4} \sim \tau c^2$ or at $\tau \sim p^3cd^3$. Properties of the different phases of semiflexible polymers are summarized in Table 1.

Table 1. Different Phases of Flexible and Semiflexible Polymers

region	osmotic pressure, Π_p	correlation Length/R_g
I	c	$N^{1/2}p^{1/2}d$
II	c	$N^{3/5}\tau^{1/5}p^{1/5}d$
IV	$c^{9/4}\tau^{3/4}p^{3/4}$	$c^{-3/4}\tau^{-1/4}p^{-1/4}d$
V	c^3	$c^{-1}p^{1/2}d$
VI	$c^2d^3\tau$	$c^{-1/2}\tau^{-1/2}p^{1/2}d$
VII	c	$N^{1/2}p^{1/2}d$

We can now address the differences between flexible and semiflexible polymers. Semiflexible polymers are more rigid than flexible polymers, and, as a result, they have a larger radius of gyration for a given N than do flexible polymers. Since the polymers are more rigid, there are fewer collisions between monomer units in a given polymer. The result is that swelling occurs at larger interactions (larger τ) in semiflexible polymers. In addition, again because polymer radii of gyration are larger, the crossover to the semidilute regions where polymers overlap occurs at a smaller concentration in semiflexible polymers than in flexible ones of the same N. In flexible polymers where $p = 1$, the point $P_2 = (p^{-3/2}N^{-1/2}, p^{3/2}N^{-1/2})$ where regions I, II, and IV meet merges with the point $P_1 = (N^{-1/2}, N^{-1/2})$ where regions I, II, VI, and VII meet. The result is that regions VI and VII completely disappear from the phase diagram of flexible polymers as shown in Figure 1c.

DNA is a semiflexible polymer with a large rigidity parameter p. The λ-DNA used in this experiment had $N_m = 48\,502$ base pairs of length $b = 0.34$ nm and width $d = 2$ nm. Its contour length is thus $L = N_mb = 16.5$ μm. Its persistence length is $l_p \approx 50$ nm, and $N_{eff} = L/2l_p = 165$. Although the hard-core width of λ-DNA is $d = 2$ nm, the salt concentration in our solutions was ~10 mM, implying an electrostatic screening length of ~3 nm. Fraden et al.[25] and others[26] have studied the effective diameter of polyelectrolyte rods (e.g., TMV) in salt solutions. They found the effective radius of the rod was approximately twice the Coulomb screening length plus the hard-core rod radius over a broad range of salt solutions that bracket our experimental conditions. Following this work we assign an effective width, d_{eff}, to the λ-DNA of 14 nm (i.e., 2 nm + 4 times the electrostatic screening length). In this case $p = 2l_p/d_{eff} \sim 7$ and $N = L/d_{eff} = 1179$. Since p is large, regions VI and VII occupy a large region of the phase diagram. As we shall see, our experiments as a function of concentration are consistent with a crossover from the dilute Gaussian phase I with $R \sim N^{1/2}$ and $\Pi \sim c/N$ to the weakly fluctuating semidilute phase VI with $\Pi \sim c^2$ and $\xi \sim c^{-1/2}$ rather than to the strongly fluctuating semidilute phase IV with $\Pi \sim c^{9/4}$ and $\xi \sim c^{-3/4}$.

B. Particle Interactions in Polymer Solutions. In this paper we focus on the interactions that arise when nonadsorbing semiflexible polymers are mixed with spherical colloidal beads. The Asakura−Oosawa model has traditionally been used to describe the depletion effect in such colloid−polymer mixtures.[3] The polymer is modeled as a hard sphere with a radius equal to the radius of gyration of the polymer, with the result that a region of depleted polymer concentration develops around the colloidal particle. The size of this region is determined by the diameter of the polymer coil. When two colloidal particles come within a polymer diameter of each other, the depleted regions start to overlap,

thereby increasing the volume available to the polymers. The resulting increased entropy of the polymers produces a decrease in free energy and an attractive interaction between particles. The effective interaction between spherical particles of diameter σ, as a function of the separation r between their centers, is

$$U(r) = -\Pi_p \frac{4\pi}{3} R_p^3 \left(\frac{\lambda}{\lambda - 1}\right)^3 \left[1 - \frac{3}{2}\frac{r}{\sigma\lambda} + \frac{1}{2}\left(\frac{r}{\sigma\lambda}\right)^3\right] \quad (3)$$
$$\sigma \le r \le \sigma + 2R_p$$

where Π_p is the polymer osmotic pressure, R_p is the effective hard-sphere radius that describes the polymer, and $\lambda = 1+2R_p/\sigma$. Polymers are of course not rigid spheres: they explore many different configurations, and their average shape is ellipsoidal rather than spherical. The actual potential should, therefore, not be identical to the AO potential. Indeed, exact calculations for a sphere near a wall in a dilute solution of Gaussian polymers[7] and simulations of two spheres in a dilute solution of hard rods[11] show systematic deviation from AO behavior. We find, however, that the AO model's functional form describes our data well provided we treat the polymer radius and the osmotic pressure as free fitting parameters.

The widely accepted Asakura−Oosawa model successfully accounts for depletion in dilute polymer−colloid mixtures, but what happens as the polymer concentration is increased? Do we have to abandon this picture in crowded macromolecular environments? In the semidilute solution, overlapping polymer coils lead to a new size scale determined by the correlation length. In this entangled regime, the depletion cavity thickness is determined by the correlation length and not the radius of gyration. The polymer solution can be viewed as a close-packed system of noninteracting spheres of size ξ, whose steric avoidance of embedded particles gives rise to the depletion effect. However, unlike the case of hard spheres, liquid structural effects are not important since the volume fraction of the polymer backbones is still very low, allowing the polymer "blobs" to interpenetrate.

Depletion effects in the semidilute region VI are often described by a mean-field theory.[5] In this regime the eigenvalue equation for the density of segments, $c(r) = \psi(r)^2$ can be written as

$$\frac{a^2}{6}\nabla^2\psi - \frac{U(r)}{k_B T}\psi = \epsilon_0\psi \quad (4)$$

where $U(r)$ represents the interaction potential between links, $a = dp^{1/2}$, and ϵ_0 is an eigenvalue. In the self-consistent mean-field approximation $U(r) = vc(r)$ where $v \approx B_c$ is the excluded volume parameter. The first term in eq 4 represents the effects due to confinement of the polymer chains, and the second term represents the interaction between the links. This equation can be solved in a confined geometry by imposing boundary conditions that the link concentration go to zero at the interface and reach the bulk value, c_{bulk}, far from the surface. The latter condition can be used to determine the eigenvalue. Moreover, eq 4 naturally leads to the definition of a correlation length, $\xi = a/(6vc_{bulk})^{1/2}$.

Solutions to eq 4 have been obtained in a wall geometry and can be extended via the Derjaguin approximation to explain the attraction between two large spherical particles. The interaction energy per unit area between two plates separated by a distance r (where $r \le \pi\xi$) is linearly related to the distance between the plates by $U/k_BT = (c_{bulk}a^2r)/12\xi^2$.[5] In the two-sphere geometry, each sphere's surface is divided into rings, and the interaction between facing rings is evaluated using this planar expression. The total interaction energy can be calculated by integrating over all the rings to yield

$$U_{MF} = \Pi_p\left[\pi\frac{\sigma}{2}(\pi\xi - \sigma - r)^2\right] \quad (5)$$

where ξ is the correlation length, and $k_BTc_{bulk}a^2/12\xi^2$ is identified with the mean-field osmotic pressure, Π_p. When $\sigma \gg R_p$, the Asakura−Oosawa model can be shown to be equivalent to eq 3 up to second order in $r - (\sigma + 2R_p)$. The equivalence can be seen by expanding the AO model around $\sigma\lambda$, which is the sum of the diameters of the two species. At this point the potential approaches zero, and Taylor expanding yields only second- and third-order terms. This allows us to rewrite eq 3 as

$$U_{AO} = -\Pi_p\frac{\pi}{4}\left[\sigma\lambda(r - \sigma\lambda)^2 + \frac{1}{3}(r - \sigma\lambda)^3\right] \quad (6)$$

Comparison of eqs 5 and 6, in the limit that $\sigma \gg 2R_p$, shows that the two models are identical to second order provided we identify R_p with $\pi\xi/2$. The importance of the third-order term in eq 6 diminishes as the particle−polymer size ratio increases. Thus the simple picture that describes depletion in hard-sphere and dilute polymer solutions can still be retained in the semidilute regime by modeling the background fluid as an ideal gas of spherical blobs with diameter $\pi\xi$.

The above mean-field treatment of depletion is valid for mixtures in which the colloidal particle is much larger than the correlation length. As the size of the bead approaches ξ, we expect that the third-order term in eq 6 will become important and that the functional dependence of the potential will reflect this change. Since the Asakura−Oosawa model relies on a geometrical overlap factor, we would expect the form of the potential to hold even when the colloidal spheres were smaller than the correlation length. However, a simple blob model for the structure of the polymer solution may breakdown on these length scales.

III. Experiments

We used a model colloid−polymer mixture to probe these interactions as a function of polymer concentration. The polymer in our experiments is bacteriophage lambda DNA (λ-DNA; New England Biolabs Inc.), which is monodisperse and has a 16.5 μm contour length. This linear DNA has a 12 base-pair overhang on both ends. These single-stranded ends were first filled-in using DNA Polymerase I[27] to prevent circularization and dimerization of the chains. The samples were then resuspended in different Tris-buffers [i.e., a buffer containing tris(hydroxymethyl)aminomethane] all containing 0.1 mM EDTA at pH = 8.0, but having ionic strengths that ranged from 0.1 mM Tris-HCl to 50 mM Tris-HCl. The concentration series was measured in a standard 10 mM TE buffer (10 mM Tris-HCl, 0.1 mM EDTA, pH = 8.0). In this buffer, λ-DNA has a persistence length of ≈50 nm[28] and a radius of gyration, measured by light scattering, of $R_g \approx 500$ nm.[29] At these salt concentrations, the Debye−Hückel screening length is ≈3 nm so that the range of the electrostatic interactions is much smaller than the entropic length scales we want to probe.

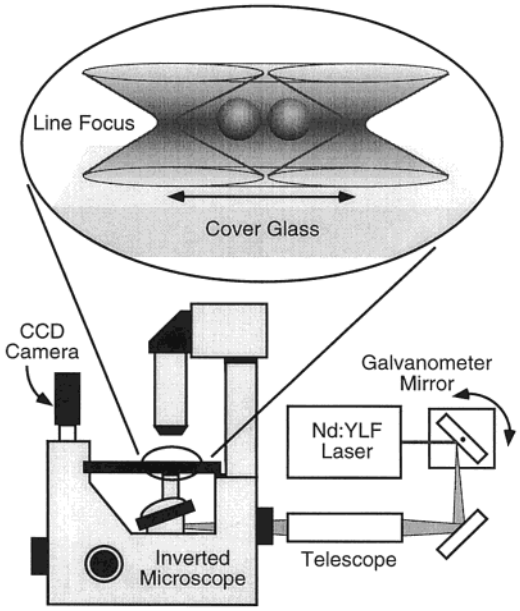

Figure 2. Experimental setup. The inset shows two spheres trapped in the scanning trap.

Our experiments on solutions of λ-DNA were carried out in concentrations ranging from 5 to 300 μg/mL, which spans both dilute and semidilute regimes (the crossover concentration is expected to be 30−50 μg/mL[30]). A very small volume fraction ($\approx 10^{-7}$) of negatively charged silica spheres of diameter 1.25 $\pm$ 0.05 μm (Bangs Laboratories Inc.) were added to the DNA to serve as our probe test spheres. At this volume fraction, a typical microscope field of view contained only about two or three silica spheres. The negative charges on both components prevented nonspecific adsorption of DNA onto the colloidal particles. This was confirmed by labeling the DNA with YOYO-1 iodide dye (Molecular Probes, Inc.) and visualizing both the particles and the DNA simultaneously with fluorescence microscopy. The samples were loaded into a 20 μL microchamber formed by sealing a microscope slide to a #1.5 coverslip with a Parafilm spacer. The samples were prepared and loaded into their chambers immediately prior to data collection.

We viewed the samples using a Zeiss Axiovert 135 inverted optical microscope with a high numerical aperture (NA = 1.4), 100× oil-immersion objective. By focusing about 50 mW of the CW output of a Nd:YLF laser (wavelength = 1054 nm) with this objective, we formed an optical tweezer. The laser beam could be scanned with a single-axis galvanometer-driven steering mirror, located at a plane conjugate to the microscope objective's back aperture, outside the microscope housing (see Figure 2 for a schematic of the experimental apparatus). This allowed the laser focus to be scanned back and forth along a line in the focal plane of the objective at 180 Hz. With such fast scanning, the colloidal spheres respond only to the time-averaged optical field, freely diffusing along the line while being strongly confined in the other two perpendicular directions. Since the laser scans are bidirectional, any small impulses imparted by the scanning trap effectively cancel out. Typically we trapped two silica spheres on the line focused 3 $\pm$ 0.5 μm from the chamber wall. This distance was chosen to minimize hydrodynamic and electrostatic wall effects, and at the same time it minimized out-of-plane motion due to weakening of the optical trap by spherical aberration. We carefully regulated the sphere−wall separation and laser power during the course of the experiment to keep trapping characteristics constant.

The effective interaction potential of the two spheres is related to the probability, $P(r)$, of finding the two spheres with centers separated by r through the Boltzmann relation, $P(r) \propto \exp(-U(r)/k_BT)$, where $U(r)$ is the interaction free energy, k_B is the Boltzmann constant, and T is the temperature. We estimate this equilibrium probability distribution from a histogram of the measured pair separations. Thirty minutes of videotape yields roughly 10^5 image fields and separation measurements for histogramming.

The motion of the beads was imaged with a CCD camera (Hitachi, model KP-M1U) at an effective magnification of 79 nm/pixel and recorded on a computer-controlled S-VHS video deck. To reduce blurring due to rapid Brownian motion, we used a 100 μs electronic shutter and a high-intensity, IR-filtered halogen lamp. Our two-dimensional video images allow us to measure a projection of the actual three-dimensional intersphere separation. However, the confinement of the spheres by the optical tweezer to the microscope's focal plane allows us to equate the measured in-plane separation and their actual three-dimensional separation. This is critical for such high spatial resolution measurements. The other essential feature of the scanned optical tweezer is that the forces it exerts on the particles along their line of centers are small enough as to not overwhelm the two spheres' own minute interactions.

We collected roughly 30 min of tape for a single pair of beads in DNA. The experiment was then repeated immediately with a DNA-free buffer sample that served as a control measurement, allowing subtraction of the trap-induced forces. Digitization and analysis were subsequently performed off-line. Processing only a small field of view around the trap (120 × 40 pixels) greatly reduces the volume of image data and speeds analysis.

The positions of the spheres were measured in each image using a centroiding technique.[31] Specifically, we calculate the brightness-weighted centroid of the sphere's image within a circular mask. Since the even and odd rows of the image are exposed at different times in interlaced (NTSC) video, the image was decomposed into two "half-frames", which were centroided separately. For an isolated particle that appears roughly 10 pixels in diameter, we are able to calculate the centroid position to roughly 5 nm along the CCD row (and laser-scanning) direction, with somewhat poorer resolution in the perpendicular direction owing to the interlacing. This resolution figure is directly related to the amount of brightness noise present in the original image and is ultimately limited by the CCD's shot and amplifier noise.[31] To avoid noise due to pixel-to-pixel gain and offset variations on the CCD chip, we employed a flat-fielding algorithm. Specifically, we recorded videotape of an empty field of view under illumination conditions identical to that of the experiment as well as at a considerably lower illumination level. The average brightness recorded in the "bright" and "dark" frames allowed us to fit for a gain and offset for each pixel. Each of the colloid images could then be "flattened" such that each pixel has the same calibrated response.

Measuring the separation of the two particles was complicated by the overlap of their diffraction blurred images when they came close to contact. Image brightness from a neighboring particle spilling into the centroid mask causes a systematic overestimation of the separations near contact. We employ a simple reflection algorithm, based on the assumption that the bead images obey linear superposition, to approximately correct for the overlap of the sphere images.[32] This was done in two processing steps (see Figure 3). For example, to find the center of the sphere I(II), we first create a new image by reflecting the entire image in Figure 3b about the axis through the center of sphere II(I). Then we subtract this reflected image from our original image. The results are shown in Figure 3c,d. The corrected center of sphere I(II) is derived by computing the centroid of the resulting parabolic feature in Figure 3c (Figure 3d). This process approximately removes additive contributions to the image distortion on sphere I(II) due to sphere II(I). The entire process is repeated once to refine the original centroid estimates. Numerical tests with artificial, linearly superposed images verify that this algorithm yields the correct pair separations to better than 10 nm all the way down to contact, whereas the conventional one overestimates the separation by roughly 80 nm at contact. When tested on actual sphere pair images, the contact separations measured

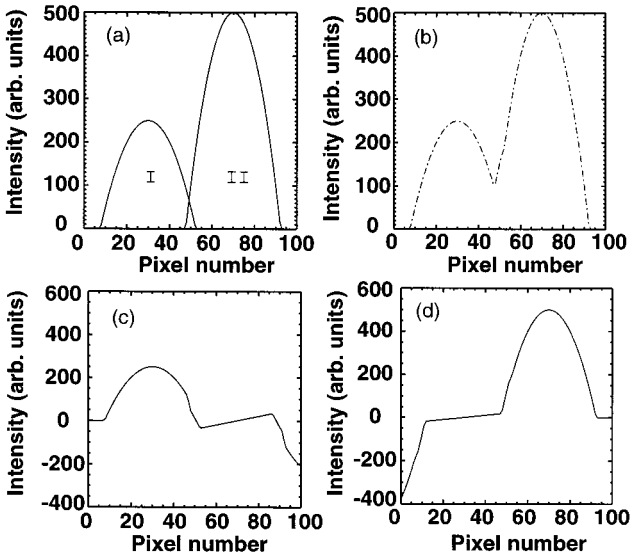

Figure 3. Schematic of the centroid-calculating algorithm used to correct for overlap. In (a) we show two spheres modeled as parabolic caps, with a small overlap region. The sum of these two parabolic functions shown in (b) closely resembles the image profile we measure. We then locate the two maxima and reflect the image around each of these points (see text). The processed images of sphere I and II are shown in (c) and (d), respectively.

by the two algorithms also differ by roughly 80 nm, suggesting that linear superposition is a reasonable approximation to the behavior of our imaging system.

In addition to the contributions from the entropic interactions we wish to study, the measured free energy in the DNA solution contains contributions from the bare interaction of the hard spheres and from optical tweezer-induced interactions. Spatial variations in the time-averaged optical intensity along the scanning direction leads to an optical cage that affects the probability distribution, $P(r)$. If this optical potential along the line is spatially independent or parabolic, this effect can be removed from the measured intersphere potential. We made independent measurements with single particles to ensure that our optical potential is very nearly parabolic. The effect of the optical cage was then determined independently by the DNA-free measurement since the optical properties (e.g., refractive index) of the DNA solution do not change noticeably over the range of concentrations used. We isolate the entropic interactions due to the DNA by subtracting off this background potential. To reduce the effects of polydispersity in the silica particles, we modeled the background potential with a smooth polynomial fit outside the repulsive core region. Figure 4 shows the steps used to obtain the final potentials.

IV. Results and Discussion

We first investigated the changes produced in the depletion potential as the DNA concentration is increased from the dilute into the semidilute regime. To obtain a large stiffness parameter p, these measurements were conducted in a 10 mM concentration TE buffer. The resulting potentials for all DNA concentrations are displayed in Figure 5. We see a long-range monotonic attraction in every case. The lower concentrations exhibit shallow potential wells and the longest-range interaction. As the concentration is increased into the semidilute regime, the potential wells get deeper, and the range contracts dramatically. Throughout the range of concentrations explored, we observe a shrinkage in the range of the well from 1μm to about 300 nm and, concurrently, an increase in well depth from 0.5 k_BT to 5 k_BT.

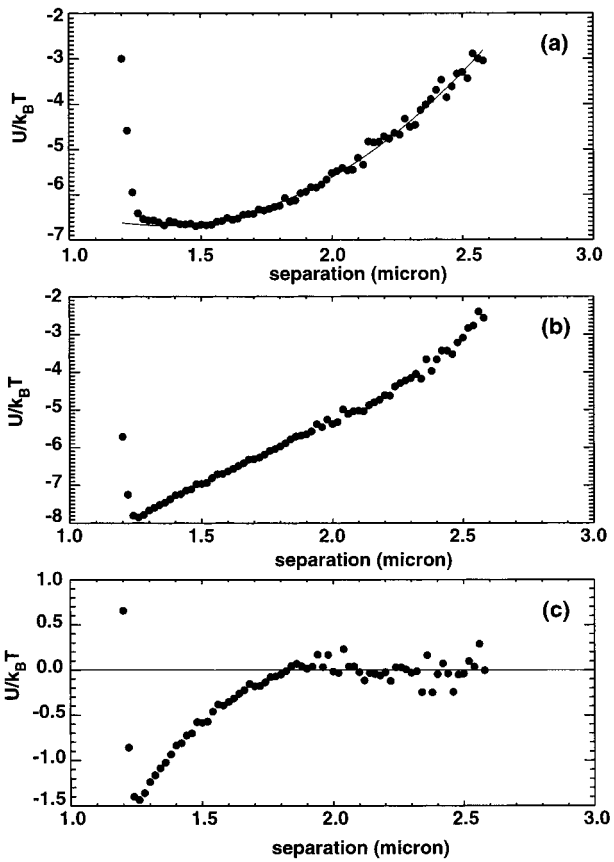

Figure 4. Raw interaction potential between two 1.25 μm silica spheres, in (a) the buffer (with a parabolic fit which is overlaid) and (b) the DNA solution. The dimensionless potential $U(r)/k_BT$ (c) is obtained by subtracting the solid line (a) from (b).

We adopt the Asakura−Oosawa (AO) depletion model to interpret our data. We fit our measured potentials with eq 3 treating Π_p and R_p as free parameters. Since our method only determines the potential up to an undetermined additive offset, we shift the potential curves vertically so that the potential at long range is zero. The fits to eq 3 are shown in Figure 5 as solid lines.

In the dilute solution the effective polymer radius R_p should equal the radius of gyration of the polymer, R_g, and the fitted osmotic pressure should depend linearly on DNA concentration, n_p (i.e., $\Pi_p = n_p k_B T$). The first three data points in Figure 6a,b correspond to the parameters of the dilute regime. The observed trends agree with the predictions for a dilute polymer solution—the effective diameter of the polymer is measured to be 1.2 ± 0.2 μm and is independent of the concentration. This value also agrees well with light-scattering measurements for R_g[29] in similar buffers. The calculated swelling parameter, which is a measure of the ratio of the actual size to the ideal expected size, $\alpha \equiv R/R_\theta = 1.15 \pm 0.2$, where $R_g = (Ll/6)^{1/2} = 0.52$, indicates that our solution lies in region I. The swelling parameter can be expressed in terms of the z parameter, $\alpha^2 = 1 + 4z/3$,[23] which from the measured α yields a z value of 0.24 ± 0.04. This further validates the assertion that the DNA lies in region I, where link interactions are small.

The osmotic pressure obtained from fitting our data to the AO model is nearly linear in $n_p k_B T$ with a slope of 0.5 ± 0.3, significantly lower than the value of unity predicted for an ideal gas of hard spheres. Since the physical osmotic pressure due to dilute DNA should be

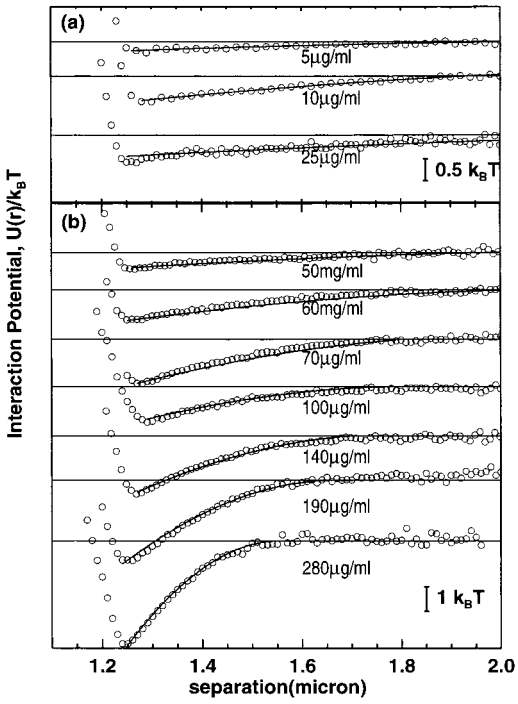

Figure 5. Interaction potential between two 1.25 μm silica spheres in (a) the dilute and (b) the semidilute region. The dimensionless potential $U(r)/k_BT$ is plotted as a function of r, the interparticle distance. The open circles represent actual data points, and the solid lines are fits to the AO model, as described in the text.

given by the ideal gas law, this deviation in the measured pressure can only represent a quantitative failure of the AO model itself. As discussed earlier, this deviation undoubtedly arises because polymers are not hard spheres. They adopt many configurations, most of which are highly anisotropic. Our measured prefactor of less than unity indicates that polymers produce a weaker depletion force than do hard spheres of equivalent size and number density. This is in agreement with simulations of the depletion force between two spheres in a dilute solution of hard rods.[11] Interestingly, exact calculations for a sphere near a wall indicate that the polymers exert a stronger depletion force than do hard spheres.[7] Given the discrepancy in the osmotic pressure emerging from the AO model, it is possible that the model's other parameter, R_g (and the inferred solvent quality α), may also be affected somewhat by the polymer anisotropy.

The relatively large error for the fit parameters in the dilute limit is a result of the shallow well depth of the interaction potentials. Since our potentials are determined up to an arbitrary constant, we add a constant to force the large separation potential to be zero as required. Long-ranged potentials decrease the accuracy with which we can determine the vertical offset. We are currently in the process of performing similar experiments on λ-DNA that has been cut in half with a restriction enzyme. This effectively reduces the chain length, increases the number density below c^*, and should allow us to accurately quantify the coil size and osmotic pressure in the dilute limit.

The behavior of the interaction potential changes dramatically in the semidilute regime. Beyond the critical concentration, a best fit to the data yields $R_p = (0.4 \pm 0.05)\ n_p^{-0.5\pm0.1}$ and $\Pi_p/k_BT = (0.8 \pm 0.2)n_p^{2.2\pm0.2}$, where R_p is measured in μm and n_p and Π_p/k_BT in $(\mu m)^{-3}$. Here n_p, the number density of polymer coils in solution, can be related to the monomer concentration through $n_p = c/N_m$, where $N_m = 48\ 502$ is the number of base-pairs in λ-DNA. The relationship between the "effective size", R_p, and n_p has a measured scaling exponent of -0.5 ± 0.1, which strongly suggests that our substitution of $(\pi/2)\xi$ for R_p in eq 1 is appropriate and that our solution lies in the weakly fluctuating semidilute regime (VI). The $-3/4$ exponent for ξ predicted for the strongly fluctuating semidilute region (V) lies outside the measurement error. However, the measured exponent of 2.2 ± 0.2 for Π_p as a function of n_p is consistent with the predictions of 2.25 for the strongly fluctuating regime as well as the value of 2 for the weakly fluctuating region. This is probably a result of the greater uncertainty associated with the well depth measurements. Taken as a whole, our data, including the observation that $z < 1$ in dilute solutions, are consistent with a crossover as a function of concentration from the dilute Gaussian chain region to the weakly fluctuating semidilute region (VI) for semiflexible polymers.

The second virial coefficient for λ-DNA is measured from the slope of the osmotic pressure data to be $B = (3.1 \pm 0.8) \times 10^{-5}\ \mu m^3$ (see Figure 1b and eq 1). This can be converted to more conventional units defined by $A_2 = N_A B N_{eff}^2/M_w^2$, which yields $A_2^{\Pi} = (4.8 \pm 1.2) \times 10^{-4}$ mol·cm^3/gm^2. This result also provides a useful consistency test of the interpretation of our data. We can compare the measured correlation length $\xi_m = (2/\pi)R_p$ with the theoretically predicted correlation length $\xi_t = l_p(6\ BN_{eff}n_p)^{-1/2}$ that can be calculated using the measured B. This predicts that $\xi_t n_p^{1/2} = 0.28 \pm 0.03\ \mu m^{1/2}$, whereas, $\xi_m n_p^{1/2} = 0.25 \pm 0.03\ \mu m^{1/2}$. These numbers agree within error estimates. In addition the measured second virial coefficient yields $z = 0.26$, which compares well with the results inferred from the dilute region.

We use the second virial coefficient to calculate a phase diagram for DNA that is shown in Figure 7. The DNA volume fractions are calculated by including the excluded volume caused by the screening length of ions in solution (i.e., we use an effective width, $d_{eff} = 14$ nm). This effectively produces a high effective volume fraction. The results yield a very large region that is dominated by the weakly fluctuating semidilute region. Region IV is reduced to a minimum and can only be accessed at solvent qualities that are much further away from the θ-point. The dashed line in Figure 7a corresponds to the solvent quality and volume fraction explored in our experiments. In Figure 7b we show a similar plot derived from assuming $d_{eff} = 8$ nm (i.e., d_{eff} = 2 nm + 2× the Debye−Hückel screening length). In both cases, the data spans from the dilute Gaussian coil region (region I) to the weakly fluctuating semidilute region (region VI).

To verify that the screening length and osmotic pressure parameters emerging from our fits were really intrinsic properties of the DNA solution, we performed a control measurement with different sized colloidal spheres. The potentials for the two different sizes, measured at a DNA concentration of 60 μg/mL, are shown in Figure 8. The values obtained for the correlation length and osmotic pressure agree within the expected errors, even though the probe spheres radii differ by 25%. This verifies that the observed depletion potential arises from polymer-induced entropic contributions and is not an artifact of the chosen sphere size.

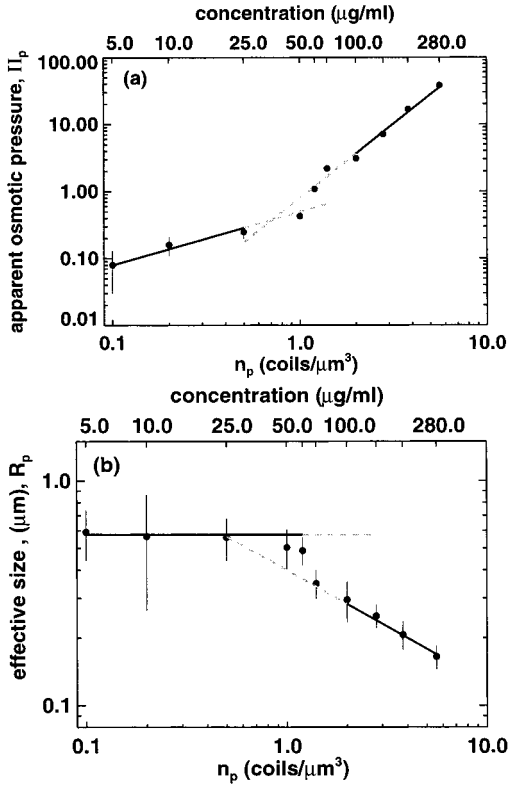

Figure 6. (a) Scaling behavior of the osmotic pressure vs the concentration. The vertical axis represents Π/k_BT, and the horizontal axis is concentration in units of number density. Similarly in (b) the filled circles represent the fit parameter R_p (we have used $\xi = (2/\pi)R_p$ in the semidilute regime) in micrometers is plotted against different polymer concentrations. The solid lines represent fits to mean-field theory predictions and are described in detail in the text. In both graphs $n_p^* \approx (4\pi/3)\ R_p^{-3} \approx 1.0\ \mu m^{-3}$ marks the crossover from the dilute to the semidilute regime.

Finally, we investigated the changes in the form of depletion attraction due to modifying the stiffness parameter p, by varying the ionic strength of the background buffer. Changes in the salt concentration lead to changes in the Debye−Hückel screening length and can be used to control the repulsive attractions between the DNA links. By decreasing the amount of monovalent salt, the range of electrostatic interactions can be increased and vice versa. The Tris-HCl salt concentration was varied from 0.1 to 50 mM, changing the screening length from 30 nm to 1 nm, and the interaction potential was measured in each of these buffers.

The potential between the two silica spheres was measured at a fixed DNA concentration in both the dilute (20 μg/mL) and the semidilute (100 μg/mL) regimes. Measurements at low salt concentrations, below 1 mM, yielded surprisingly short-ranged potentials (see Figure 9). In this regime, the range decreased with decreasing salt concentration in both the dilute and the semidilute polymer solutions. No significant changes were observed for salt concentrations between 1 and 50 mM (see Figure 10) at either DNA concentration. For the purposes of this paper (which uses 10 mM salt solutions in the majority of the measurements), our observation that the potentials are approximately constant around 10 mM ensures that our conclusions will be insensitive to small errors associated with solution salt concentrations. On the other hand, it is worthwhile to reflect on the apparently anomalous increase of and

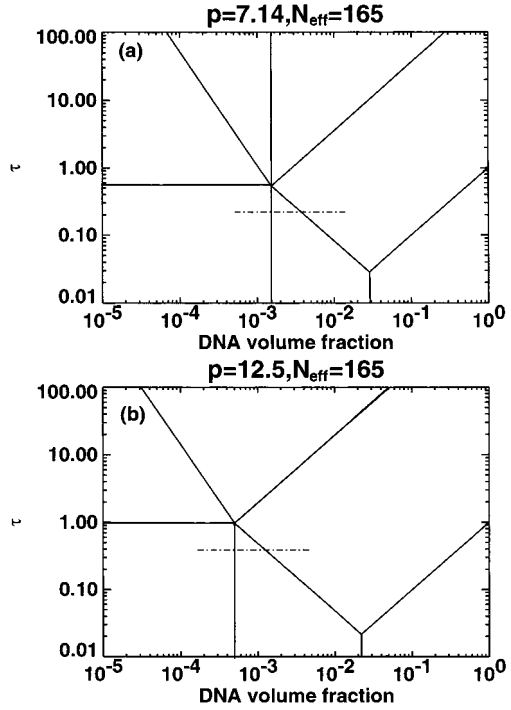

Figure 7. Phase diagram for λ-DNA. We use $N_{eff} = 165$ and two values of the rigidity parameter, (a) $p = 7.14$ and (b) $p = 12.5$, to calculate the above diagram. The dashed line represents the region explored in our experiment calculated using $\tau = B/l_p^2 d_{eff}$. We use the measured value, $z = 0.25$, to calculate τ using the relationship $\tau = (z/2)(2\pi/3)^{3/2}N^{-1/2}p^{3/2}$ (note, $N = N_{eff}p$).

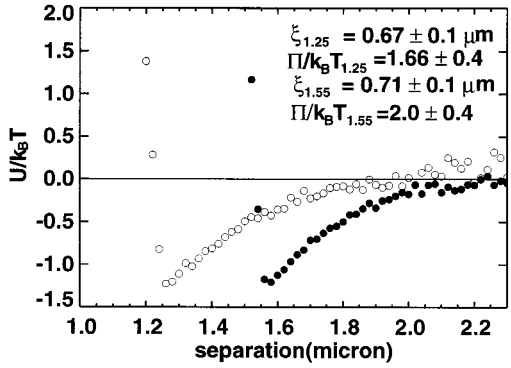

Figure 8. Polymer depletion with two different sized colloidal spheres. The filled circles represent measurements made with a 1.55 μm silica sphere in a 60 μg/mL DNA solution. The open circles are measured at the same concentration except the sphere size used was 1.25 μm. In both cases the correlation length is measured to be close to 700 nm and Π/k_BT is given by 1.66 ± 0.4 μm^{-3} and 2.0 ± 0.4 μm^{-3} for the 1.25 and 1.55 μm spheres, respectively.

plateau in the range of the interparticle potential as a function of increasing salt concentration. In the dilute polymer limit, the persistence length has been observed to increase with decreasing salt.[33] At the same time the effective diameter and polymer volume fraction increase with decreasing salt. Evidently these effects must compete to give rise to our observations. Further experiment will be required to clarify these issues.

V. Conclusions

To summarize, we measured the interaction potentials for a colloid−polymer mixture consisting of anionic

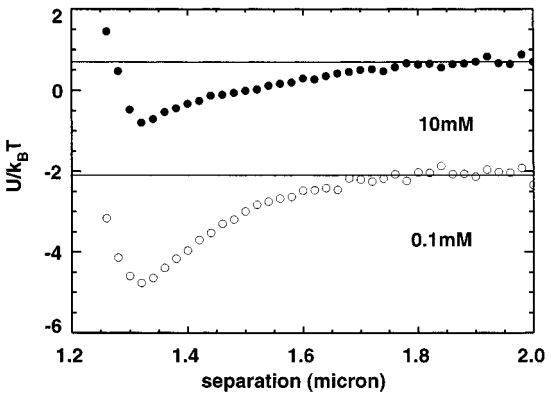

Figure 9. Two interaction potentials measured at (a) 10 mM monovalent salt concentration and (b) 0.1 mM. Both potentials are measured in the semidilute region at a DNA concentration of (100 μg/mL).

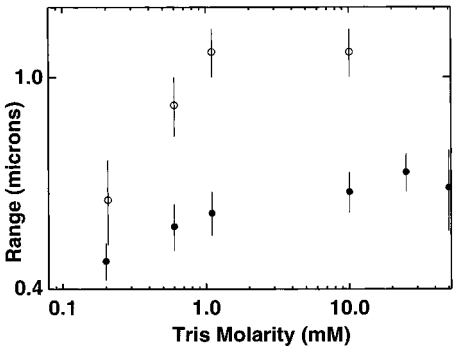

Figure 10. Effect of ionic strength on the range of the potential $2R_p$. The horizontal axis shows the different salt concentrations, and the vertical axis shows $2R_p$ in micrometers. The open circles represent measurements made in dilute DNA solutions (20 μg/mL), and the filled circles represent measurements in the semidilute regime (100 μg/mL).

silica particles and λ-DNA polymer. A line optical tweezer was used to confine two silica particles in a background DNA solution. Digital video microscopy techniques was used to measure the particle separations in the plane. The resulting potentials are the first simultaneous measurements of the range and depth of the interaction potential between two colloidal particles in a polymer solution of varying concentration, including a regime where the semiflexible chains are strongly entangled. The range of the measured interaction potentials was found to be related to the radius of gyration of the polymer in the dilute regime and to the correlation length in the semidilute region. The depth of the potentials was found to increase linearly with concentration in dilute DNA solutions; however, a near quadratic dependence was observed after the overlap concentration was exceeded. In both concentration regimes the Asakura−Oosawa model could be successfully used to fit the interaction potentials. As expected the dilute region can be envisioned as a solution consisting of polymer coils that act as hard spheres of size R_g. Surprisingly, the model can be extended into the semidilute region, where the polymer solution can be described as a gas of uncorrelated hard spheres with an effective diameter of $\approx\pi\xi$.

The colloidal particles also act as a gentle probe that monitors the polymer behavior in solution. Our observations present strong evidence for transitions from a dilute solution of Gaussian coils to a semidilute regime that is dominated by pair-wise contacts and is predicted to exist to only for semiflexible polymers. Moreover, our analysis allows us to measure the solvent quality for double-stranded DNA in a TE buffer. Changes to the solvent quality brought about through changes in the ionic strength show anomalous behavior at low salt concentrations.

Our *model-independent* potentials serve as an exemplar for the microscopic investigation of a broad range of questions that commonly arise in colloid−polymer solutions. Most importantly, they provide a functional form for the interactions that are inherent in these suspensions. They also highlight the important role that polymer phases play in driving depletion. The comparable size ratio of the colloid and the DNA used in our experiments also ventures into a previously unexplored regime that often arises in mixtures of nanometer-scale colloids and polymers. The technique we have demonstrated provides an effective way of probing colloidal interactions in complex fluid backgrounds. It opens up possibilities for future investigations into the fluctuation spectrum of polymers.

Acknowledgment. We thank Ben Goodrich, Zigurts Majumdar, P. D. Kaplan, V. Trappe, R. Kamien, M. Triantafillou, and D. Weitz for their helpful discussions. We also thank Elizabeth Geiger for help in DNA sample preparation. Support for this work was provided by the NSF Grant No. DMR 96-23441 (A.G.Y.) and MRSEC Grant No. DMR 96-32598 (A.G.Y. and T.C.L.).

References and Notes

(1) Russel, W. B.; Saville, D. A.; Schowalter, W. R. In *Colloidal Dispersions*; Cambridge University Press: Cambridge, England, 1989.
(2) Verma, Ritu; Crocker, J. C.; Lubensky, T. C.; Yodh, A. G. *Phys. Rev. Lett.* **1998**, *81*, 4004−4007.
(3) Asakura, S.; Oosawa, S. *J. Polym. Sci.* **1958**, *33*, 183−184.
(4) Vrij, A. *Pure Appl. Chem.* **1976**, *48*, 471−483.
(5) Joanny, J. F.; Leibler, L.; DeGennes, P. G. *J. Polym. Sci.* **1979**, *17*, 1073−1084.
(6) Eisenrielgler, E.; Hanke, A.; Dietrich, S. *Phys. Rev. E* **1998**, *54*, 1134−1152. Hanke, A.; Eisenriegler, E.; Dietrich, S. *Phys. Rev. E* **1999**, *59*, 6853−6878.
(7) Eisenrielger, E.; Hanke, A.; Dietrich, S. *Phys. Rev. E.* **1997**, *55*, 3116−3123. Bringer, A.; Eisenriegler, A.; Schlesener, P.; Hanke, A. Unpublished.
(8) Odijk, T. *J. Chem. Phys.* **1997**, *106*, 3402−3406.
(9) Schaink, H. M.; Smit, J. A. M. *J. Chem. Phys.* **1997**, *107* (3), 1004−1015.
(10) Meijer, E. J.; Frenkel, S. *J. Chem. Phys.* **1994**, *100*, 6873−6887.
(11) Kamien, R. D.; Triantafillou, M. *Phys. Rev. E* **1999**, *59*, 5621−5624.
(12) Chatterjee, A. P.; Schweizer, K. S. *J. Chem. Phys.* **1998**, *109*, 10464−10476.
(13) Chatterjee, A. P.; Schweizer, K. S. *J. Chem. Phys.* **1998**, *109*, 10477−10488.
(14) Richmond, P.; Lal, M. *Chem. Phys. Lett.* **1974**, *24*, 594−596.
(15) Lekkerkerker, H. N. W.; Poon, W. C.-K.; Pusey, P. N. Stroobants, A.; Warren, P. B. *Europhys. Lett.* **1992**, *20*, 559−564.
(16) Ohshima, Y. N.; Sakagami, H.; Okumoto, K.; et al. *Phys. Rev. Lett.* **1997**, *78*, 3963−3966.
(17) Kekicheff, P.; Nallet, F.; Richetti, P. *J. Phys. II* **1994**, *4*, 735−741.
(18) Rudhart, D.; Bechinger, C.; Leiderer, P. *Phys. Rev. Lett.* **1998**, *81*, 1330−1333.
(19) Milling, A. J.; Biggs, S. *J. Colloid Interface Sci.* **1995**, *170*, 604−606.
(20) Ye, X.; Narayanan, T.; Tong, P.; Huang, J. S. *Phys. Rev. Lett.* **1996**, *76*, 4640−4643. Ye, X.; et al. *Phys. Rev. E* **1996**, *54*, 6500−6510.
(21) Evans, E.; Needham, D. *Macromolecules* **1988**, *21*, 1822−1831.

(22) Schaefer, D. W.; Joanny, J. F.; Pincus, P. *Macromolecules* **1980**, *13*, 1280−1289.
(23) Grosberg, A. Y.; Khokhlov, A. R. In *Statistical Physics of Macromolecules*; AIP Press: New York, 1994.
(24) DeGennes, P.-G. In *Scaling Concepts in Polymer Theory*; Cornell University Press: Ithaca, NY, 1979.
(25) Fraden, S.; Maret, G.; Caspar, D. L. D. *Phys. Rev. E* **1993**, *48*, 2816−2837.
(26) Stroobants, A.; Lekkerkerker, H. N. W.; Odijk, T. *Macromolecules* **1986**, *19*, 2232−2238. Smith; Wooling *J. Chem. Phys.* **1970**, *52*, 953−960.
(27) Sambrook, J.; Fritsch, E. F.; Maniatis, T. In *Molecular Cloning—A lab manual*, 2nd ed.; Cold Spring Harbor Laboratory Press: New York, 1989.
(28) Taylor, W. H.; Hagerman, P. J. *J. Mol. Biol.* **1990**, *212*, 363−376.
(29) Schmidt, R. L. *Biopolymers* **1973**, *12*, 1427−1430. Dauson, J. R.; Harpst, J. A. *Biopolymers* **1971**, *10*, 2499. Arutyunyan, A. V.; Ivanova, M. A.; Kurlyand, D. I.; Noskin, V. A. *Mol. Biol.* **1993**, *27*, 705−712.
(30) Pernodet, N.; Tinland, B. *Biopolymers* **1997**, *42*, 471−478.
(31) Crocker, J. C.; Grier, D. G. *J. Colloid Interface Sci.* **1996**, *179*, 298−310.
(32) Crocker, J. C.; Dinsmore, A. D.; Matteo, J.; Yodh, A. G. *Phys. Rev. Lett.* **1999**, *82*, 4352−4355.
(33) Baumann, C. G.; Smith, S. B.; Bloomfield, V. A.; Bustamante, C. *Proc. Natl. Acad. Sci. U.S.A.* **1997**, *96*, 6185−6190.

MA990362V